Cosmological boost factor for dark matter annihilation at redshifts of $z = 10 - 100$ using the power spectrum approach

Ryuichi Takahashi[1,*] and Kazunori Kohri[2,3,4]

[1]*Faculty of Science and Technology, Hirosaki University, 3 Bunkyo-cho,*
Hirosaki, Aomori 036-8561, Japan
[2]*Institute of Particle and Nuclear Studies, KEK, 1-1 Oho, Tsukuba, Ibaraki 305-0801, Japan*
[3]*The Graduate University for Advanced Studies (SOKENDAI), 1-1 Oho,*
Tsukuba, Ibaraki 305-0801, Japan
[4]*Kavli IPMU (WPI), UTIAS, The University of Tokyo, Kashiwa, Chiba 277-8583, Japan*

We compute the cosmological boost factor at high redshifts of $z = 10$–100 by integrating the nonlinear matter power spectrum measured from high-resolution cosmological *N*-body simulations. An accurate boost factor is required to estimate the energy injection from dark matter annihilation, which may affect the cosmological reionization process. We combined various box-size simulations (side lengths of 1 kpc–10 Mpc) to cover a wide range of scales, i.e., $k = 1$–10^7 Mpc^{-1}. The boost factor is consistent with the linear theory prediction at $z \gtrsim 50$ but strongly enhanced at $z \lesssim 40$ as a result of nonlinear matter clustering. Although dark matter free-streaming damping was imposed at $k_{\rm fs} = 10^6$ Mpc^{-1} in the initial power spectrum, the damping disappears at later times of $z \lesssim 40$ as a result of the power transfer from large to small scales. Because the simulations do not explore very small-scale clustering at $k > 10^7$ Mpc^{-1}, our result is a *lower bound* on the boost factor at $z \lesssim 40$. A simple fitting function of the boost factor is also presented.

I. INTRODUCTION

In the standard cold dark matter model, cosmological structure formation is driven by the gravitational force of dark matter. The nature of dark matter remains elusive but may comprise unknown elementary particles (e.g., [1]). The annihilation of dark matter particles may generate high-energy photons or particles (such as e^+e^- and $q\bar{q}$). At the photon decoupling epoch (at $z \approx 1000$), the dark matter density was nearly homogeneous; however, at later times, the density contrast evolved and high density regions (such as halos) formed, where the annihilation is enhanced. The high-energy photon production and inter-galactic medium heating from the annihilation at high redshifts of $z \gtrsim 6$ could affect the cosmological reionization process [2–6]. Recently, the EDGES experiment reported the first detection of an absorption signature in radio signals at $z = 17$ [7], which indicates a lower gas temperature than the background radiation. This measurement can constrain (or exclude) the energy injection from dark matter annihilation [8–11].

The annihilation rate is proportional to the square of the dark matter density; therefore, an inhomogeneous density will enhance dark matter annihilation. Let us denote the dark matter density at a comoving coordinate $\boldsymbol{x}$ and a redshift z as $\rho(\boldsymbol{x}; z)$. This density can be decomposed into its spatial mean $\bar{\rho}(z)$ and its density contrast $\delta(\boldsymbol{x}; z)$ such that $\rho(\boldsymbol{x}; z) = \bar{\rho}(z)[1 + \delta(\boldsymbol{x}; z)]$. Because the collision rate is proportional to ρ^2, its spatial average over the Universe is

$$\langle \rho^2(\boldsymbol{x}; z) \rangle = \bar{\rho}^2(z) B(z), \tag{1}$$

where the cosmological boost factor is defined as $B(z) \equiv 1 + \langle \delta^2(\boldsymbol{x}; z) \rangle$.

Two methods have been used to calculate $B(z)$: the halo-model approach (e.g., [12–17]) and the power spectrum (PS) approach [18,19]. Both approaches give consistent results (e.g., Fig. 1 in Ref. [20]). In the former approach, the boost factor for a single halo is calculated and all the contributions from multiple halos for the given model parameters, such as the halo density profile and the mass function (e.g., [21]), are summed. However, there are several known uncertainties, including the ellipticity of the halo shape, inner density profile, halo mass function, subhalo (and sub-subhalo) abundance, and baryonic feedback effects. In fact, substructure clumps enhance dark matter annihilation [22–27] and gas cooling increases the central density of the halos [28–30]. This makes theoretical modeling very complicated. Furthermore, the model predictions (such as the mass function and density profile)

*takahasi@hirosaki-u.ac.jp

103518-1

must be extrapolated to very small scales that cannot be resolved by current (or even near-future) numerical simulations. These model uncertainties cause orders of magnitude variations in $B(z)$ (e.g., [31–33]).

In the latter approach, $B(z)$ is obtained by integrating the matter PS with respect to the wave number of the density fluctuations. This approach, first proposed by Refs. [18,19], is much simpler and has fewer uncertainties (such as very small-scale clustering and baryonic effects) than the former approach. References [18,19] calculated $B(z)$ to estimate extragalactic gamma-ray flux from dark matter annihilation at $z = 0$–6. They prepared the nonlinear PS using several methods: a fitting formula (Halofit [34,35]), the stable clustering ansatz [36], and Millennium Simulations I and II [37,38]. They extrapolated the analytical PS to very small scales and then integrated the PS up to the free-streaming scale of dark matter ($\sim 10^7$ Mpc^{-1}).

In this paper, we calculate $B(z)$ at redshifts of $z = 10$–100 using the matter PS measured from high-resolution cosmological N-body simulations. We run different box-size simulations (with cubic-box side lengths of $L = 1$ kpc, 10 kpc, 100 kpc, 1 Mpc, and 10 Mpc) to cover a wide range of scales up to $k = 1.6 \times 10^7$ Mpc^{-1}. These are dark matter only (DMO) simulations; however, the baryonic effect is included in the initial PS. The simulations follow nonlinear evolution near the free-streaming scale, which is set to $k_{\mathrm{fs}} = 10^6$ Mpc^{-1}. Therefore, our analysis does not rely on extrapolation beyond the free-streaming scale.

There has been several studies of first halo formation near the free-streaming scale using N-body simulations [39–41]. These studies indicate that Earth-mass halos with $\approx 10^{-6}$ $M_\odot [k_{\mathrm{fs}}/(10^6$ Mpc$^{-1})]^{-3}$ form at $z \approx 30$. Recently, Ref. [42] performed multiscale zoom-in simulations at $z = 0$ covering the halo-mass range from 10^{-6} $M_\odot$ to 10^{15} $M_\odot$. The primary interest of these studies was the halo properties, such as the mass function and density profile. As far as we know, no one has studied the nonlinear evolution of the PS near the free-streaming scale.

The rest of this paper is organized as follows. Section II discusses the cosmological boost factor in the PS approach and our simulation setting. Section III presents our main results: the nonlinear matter PS measured from the simulations and the resulting boost factor. Section IV discusses the effects of density fluctuations larger than the simulation box, the small-scale PS in the halo model, and baryonic effects on PS. Section V summarizes our study.

Throughout this paper, we adopt a cosmological model consistent with the Planck 2015 best-fit flat Λ cold dark matter model [43]: a matter density of $\Omega_m = 1 - \Omega_\Lambda = 0.3089$, a baryon density of $\Omega_b = 0.0486$, a Hubble parameter of $h = 0.6774$, a spectral index of $n_s = 0.9667$, and an amplitude of matter density fluctuations on the scale of $8h^{-1}$ Mpc $\sigma_8 = 0.8159$.

II. COSMOLOGICAL BOOST FACTOR

This section introduces the PS approach (Sec. II. A) and then discusses the linear PS (Sec. II. B) and our N-body simulation settings (Sec. II. C).

A. PS approach

Let us denote the Fourier transform of the dark matter density fluctuations as $\tilde{\delta}(\boldsymbol{k}; z)$, where $\boldsymbol{k}$ is the wave vector in the comoving scale. Then, the matter PS is defined as $\langle \tilde{\delta}(\boldsymbol{k}; z) \tilde{\delta}(\boldsymbol{k}'; z) \rangle \equiv (2\pi)^3 P(k; z) \delta_{\mathrm{D}}(\boldsymbol{k} + \boldsymbol{k}')$, where δ_{D} is the Dirac delta function. The dimensionless matter PS is defined as $\Delta^2(k; z) \equiv k^3 P(k; z)/(2\pi^2)$. Then, using the Fourier transform, the cosmological boost factor at a redshift z is [18,19]

$$B(z) = 1 + \int_0^\infty d \ln k \Delta^2(k; z). \qquad (2)$$

In the linear theory, because $\Delta_{\mathrm{L}}^2(k; z) \propto k^{n_s+3}$ in the low-k limit and $\Delta_{\mathrm{L}}^2(k; z) \to 0$ in the high-k limit (over the free-streaming scale), the integral in Eq. (2) converges. However, in the nonlinear regime, N-body simulations are required to obtain $\Delta^2(k; z)$ in the high-k regime; this is discussed in the following sections.

B. Linear PS

The linear matter PS is written as

$$P_{\mathrm{L}}(k; z) = A \left(\frac{k}{k_*} \right)^{n_s} D_+^2(z) T^2(k; z) D_{\mathrm{fs}}^2(k), \qquad (3)$$

where $k_* = 0.05$ Mpc^{-1} is the pivot scale and $D_+(z)$ is the linear growth factor, which is safely approximated as $D_+(z) \propto (1 + z)^{-1}$ in the redshift range of $z = 10$–100. The amplitude A and the spectral index n_s are set to be consistent with the Planck 2015 result [43]. Here, we do not consider the running (or the running of running) of the spectral index.

$T(k; z)$ is the transfer function for the total matter density (i.e., dark matter and baryons). Here, we use the fitting function $T(k; z)$ given in Appendix C of Ref. [44], obtained from cosmological perturbation theory.[1] In their study, the Boltzmann equation was numerically solved and the results were fitted down to a very small scale ($k = 10^4$ Mpc^{-1}). The quoted accuracy of the fitting formula is a few percent (10%) for $k = 1$–100 Mpc^{-1} ($k > 100$ Mpc^{-1}). We confirmed that their $T(k; z)$ agrees with the CAMB output [46] within 8% for $k < 10^4$ Mpc^{-1}. At small $k (\lesssim 0.1$ Mpc$^{-1})$, the $T(k; z)$ is consistent with the Bardeen-Bond-Kaiser-Szalay formula [47] with the baryonic correction [48].

---

[1] There is a minor typo in their formula [45]. In their Appendix C, α_1 should be replaced with $\alpha_1 = [1 - (1 + 24\Omega_c/\Omega_m)^{1/2}]/4$, where $\Omega_c = \Omega_m - \Omega_b$.

After the decoupling epoch, the baryonic gas pressure suppresses the growth of density fluctuations smaller than the Jeans length. As time continues, the gas temperature (and pressure) decreases, and thus, the Jeans length decreases. Therefore, the transfer function depends on the redshift (i.e., the suppression is more significant for lower z; see also Fig. 5 in Ref. [44]). Because we are interested in the matter clustering at $z \approx 10$, we used the transfer function at $z = 10$, $T(k; z = 10)$, throughout this paper. In this case, $P_L(k; z)$ simply evolves in proportion to $D_+^2(z)$.

The damping factor due to the dark matter free-streaming, $D_{fs}^2(k)$, is taken from [49]:

$$D_{fs}(k) = \left[1 - \frac{2}{3}\left(\frac{k}{k_{fs}}\right)^2\right] \exp\left[-\left(\frac{k}{k_{fs}}\right)^2\right], \quad (4)$$

for $k < \sqrt{3/2}k_{fs}$, and $D_{fs}(k) = 0$ otherwise. Throughout this paper, the free-streaming scale is set to $k_{fs} = 10^6$ Mpc^{-1}, which corresponds to a kinetic decoupling temperature of $T_d \approx 1$ MeV for dark matter particles (e.g., [49,50]). Note that the primordial PS is currently measured up to $k \simeq 0.2$ Mpc^{-1} by Planck [51], and therefore the linear PS in Eq. (3) relies on an extrapolation up to k_{fs}.

The dimensionless linear PS, $\Delta_L^2(k; z)$, is plotted in Fig. 1. The suppression at $k \gtrsim 10^3$ Mpc^{-1} is caused by the Jeans effect after the decoupling epoch (see also Fig. 4 in Ref. [44]). This scale is determined by the Jeans length λ_J just after the decoupling epoch: $\lambda_J = 2\pi/k_J$, where $k_J = 9 \times 10^2 (\Omega_m h^2)^{1/2}$ Mpc^{-1} [44]. Even at $z = 10$, the amplitude of Δ_L is less than unity over the entire k range. For the
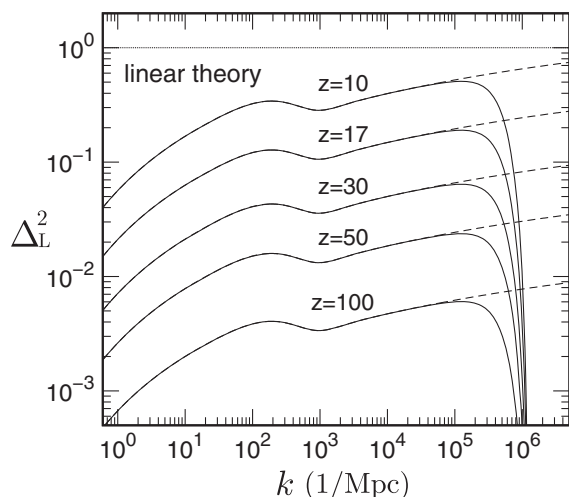

FIG. 1. Dimensionless linear matter power spectrum at $z = 10$–100. Solid curves include free-streaming damping at $k_{fs} = 10^6$ Mpc^{-1}, whereas dashed curves exclude free-streaming damping. The suppression at $k \gtrsim 10^3$ Mpc^{-1} is caused by the baryon gas pressure (i.e., the Jeans effect) after the decoupling epoch [44].

quasinonlinear regime ($\Delta_L \gtrsim 0.1$), N-body simulations are required to follow the nonlinear evolution.

C. N-body simulations

To obtain the nonlinear Δ^2, we ran N-body simulations in cubic boxes to follow the gravitational evolution of collisionless particles. These are dark matter only simulations (i.e., without nonlinear baryonic processes such as star formation, gas cooling, or radiative transfer). However, the baryonic effects in the initial linear PS (such as the baryon acoustic oscillation and the Silk damping) are included. Baryonic effects on the nonlinear PS are discussed in Sec. IV.C. Because the length scales of interest are broad, $k = 1$–10^7 Mpc^{-1}, we combined five different box-size simulations with side lengths of $L = 1$ kpc, 10 kpc, 100 kpc, 1 Mpc, and 10 Mpc. The number of particles in each box was $N_p = 5120^3$ and 2560^3 for the high-resolution (HR) and low-resolution (LR) runs, respectively. These different resolution runs were used to check the numerical convergence, given the finite spatial resolution. The minimum wave number was $k_{min} = 2\pi/L$, which is necessarily smaller than k_{fs} to include the initial power at $k < k_{fs}$. The simulation results are reliable up to the particle Nyquist wave number, given by $k_{Ny} \equiv (\pi/L)N_p^{1/3}$. Our simulation settings, including the values of L, N_p, k_{min}, k_{Ny}, and the N-body particle mass m_p, are summarized in Table I. The particle mass in the smallest box ($\simeq 3 \times 10^{-11} M_\odot$) is small enough to resolve the minimum halo mass determined by k_{fs} (i.e., Earth mass $\sim 10^{-6} M_\odot$).

The initial particle positions were given with the grid-based configuration on the basis of the second-order Lagrangian perturbation theory [52–54] at $z = 400$. The initial PS in Eq. (3) was obtained at $z = 10$ and then scaled back to the initial epoch ($z = 400$) using the linear growth factor. We used a tree-particle-mesh code, GreeM [55], to follow the nonlinear gravitational evolution. The gravitational softening length was set to 5% of the mean particle separation. The number of particle-mesh grid cells was set to $N_p/8$ in all the runs.

The particle position data were stored at $z = 10, 17, 23, 30, 40, 50, 60$, and 100. To measure the density contrast $\delta(x; z)$, we assigned the particles to the 2816^3 grid cells in the box using the cloud-in-cell interpolation (e.g., [56,57]). Then, the Fourier transform of $\delta(x; z)$ was obtained using a fast Fourier transform.[2] To explore smaller scales, we applied the folding method [58], which folds the particle positions x into a smaller box of side length L/n by replacing x with $x\%(L/n)$, where $a\%b$ is the reminder of a/b. Here, we set $n = 10$ and 100. This procedure effectively increases the spatial resolution by n times.

---

[2]FFTW3 (the Fastest Fourier Transform in the West) at http://www.fftw.org/.

TABLE I. Summary of our N-body simulations: the side length of cubic simulation box L, the number of particles N_p, the minimum wave number $2\pi/L$, the particle Nyquist wave number $k_{\mathrm{Ny}} \equiv (\pi/L)N_p^{1/3}$, and the N-body particle mass m_p. Values in parentheses indicate differing values for the low-resolution runs.

L	N_p	$2\pi/L$ [Mpc^{-1}]	k_{Ny} [Mpc^{-1}]	$m_p[M_\odot]$
10 Mpc	5120^3 (2560^3)	0.63	1.6×10^3 (800)	29 (230)
1 Mpc	5120^3 (2560^3)	6.3	1.6×10^4 (8.0×10^3)	2.9×10^{-2} (0.23)
100 kpc	5120^3 (2560^3)	63	1.6×10^5 (8.0×10^4)	2.9×10^{-5} (2.3×10^{-4})
10 kpc	5120^3 (2560^3)	630	1.6×10^6 (8.0×10^5)	2.9×10^{-8} (2.3×10^{-7})
1 kpc	5120^3 (2560^3)	6.3×10^3	1.6×10^7 (8.0×10^6)	2.9×10^{-11} (2.3×10^{-10})

The PS estimator was measured as

$$\hat{P}(k;z) = \frac{1}{N_{\mathrm{mode}}} \sum_{|\boldsymbol{k}'|\in k} |\tilde{\delta}(\boldsymbol{k}';z)|^2, \qquad (5)$$

where N_{mode} is the number of Fourier modes in a spherical shell of $k - \Delta k/2 < |\boldsymbol{k}'| < k + \Delta k/2$. The bin width was set to $\Delta \log_{10} k = 0.2$. We did not subtract the Poisson shot noise, $P_{\mathrm{sn}} = L^3/N_p$, from the measured $P(k;z)$ because this simple formula P_{sn} is inaccurate, especially for high z (see, e.g., Secs. 4 and 6.2 in Ref. [59]).

To reduce the sample variance for the HR runs, we employed the "pairing and fixing" technique [60,61] in which paired simulations are prepared in each run. In the initial condition for both of the paired runs, the amplitudes of the density contrasts in the Fourier space are given to reproduce the input $P_{\mathrm{L}}(k;z)$ without Gaussian randomization [i.e., $|\tilde{\delta}(\boldsymbol{k})| = P_{\mathrm{L}}^{1/2}(k;z)$]. The phase, $\theta(\boldsymbol{k}) = \arg[\tilde{\delta}(\boldsymbol{k})]$, for one of the paired runs is randomly chosen in a range of $0 - 2\pi$, whereas the phase is set to $-\theta(\boldsymbol{k})$ for the other run (i.e., these phases are opposite to each other). Accordingly, the mean PS of the paired runs agrees with the ensemble average of many Gaussian realizations even in the nonlinear regime [61]. For the LR runs, we prepared four independent realizations with different seeds for the Gaussian initial condition.

III. RESULTS

This section presents the simulation results for the nonlinear PS (Sec. III A) and the resulting boost factor (Sec. III B).

A. Nonlinear PS

Figure 2 shows a plot of $\Delta^2(k;z)$ measured from the simulations with various box sizes ($L = 1$ kpc–10 Mpc), as denoted by the different colored symbols. Here, the results are the averages from the paired simulations (the four realizations) for the HR (LR) runs. The plotting range is from $k = k_{\mathrm{Ny}}/10$ to k_{Ny}, as given in Table I, for the HR runs. Only for $L = 1$ kpc, the results are plotted up to $k = 10^8$ Mpc^{-1} ($\simeq 6k_{\mathrm{Ny}}$). The range is the same for the LR runs,

but the maximum wave number is the LR k_{Ny}, which is half the HR k_{Ny}. Only for $L = 10$ Mpc, the minimum wave number is 5.3 Mpc^{-1}, where the relative Gaussian variance of $P(k;z)$ [$\equiv (2/N_{\mathrm{mode}})^{1/2}$ in Eq. (5)] is less than 3%.

As seen in the figure, at $z = 60$, the simulation results agree fairly well with the linear theory. At $z \simeq 40$, the nonlinear evolution starts at $k \gtrsim 10^3$ Mpc^{-1}. According to previous studies (e.g., [39,40]), the first halos with Earth mass $\approx 10^{-6}$ $M_\odot[k_{\mathrm{fs}}/(10^6$ Mpc$^{-1})]^{-3}$ formed around this epoch. At $z = 10$, Δ^2 is approximately 100 times larger than the linear theory at $k \gtrsim 10^3$ Mpc^{-1}. The HR and LR runs are consistent in the plotting ranges of the scales and redshifts. It is known for the initial PS with a small-scale damping that unphysical small halos below the free-streaming scale are formed from spurious fragmentation of filaments owing to a finite mass resolution [62–65]. These halos may affect the nonlinear PS at $k \gtrsim k_{\mathrm{fs}}$. However, the agreement between the HR and LR results suggests that this can be negligible up to the LR k_{Ny}. The discontinuities between the larger and smaller boxes are due to the lack of density fluctuations larger than the smaller box size. The large-scale power deficit suppresses small-scale clustering because the power transfers from large to small scales via the mode coupling between the different scales [66–70]. In other words, our small box simulations give lower bounds on Δ^2 (the effect of density fluctuations larger than the box size are discussed in Sec. IV A).

The free-streaming damping at $k_{\mathrm{fs}} = 10^6$ Mpc^{-1} imposed in the initial conditions persist at $z \gtrsim 50$. However, at $z = 40$ and later, this feature disappears. For example, the results with and without initial damping, denoted by the red and the gray circles, respectively, become similar at lower z. This is because the power flow from large to small scales erases the damping feature. This trend is also observed in the nonlinear evolution of the free-streaming damping for warm dark matter [71–76]. The disappearance of the damping has important implications for $B(z)$ because the integration in Eq. (2) does not appear to converge in the high-k limit.

The red dotted lines in Fig. 2 indicate the shot noise, $\Delta_{\mathrm{sn}}^2 = (L^3/N_p)[k^3/(2\pi^2)]$, for the red circles. The simulation results do not approach these lines at $k < k_{\mathrm{Ny}}$, which
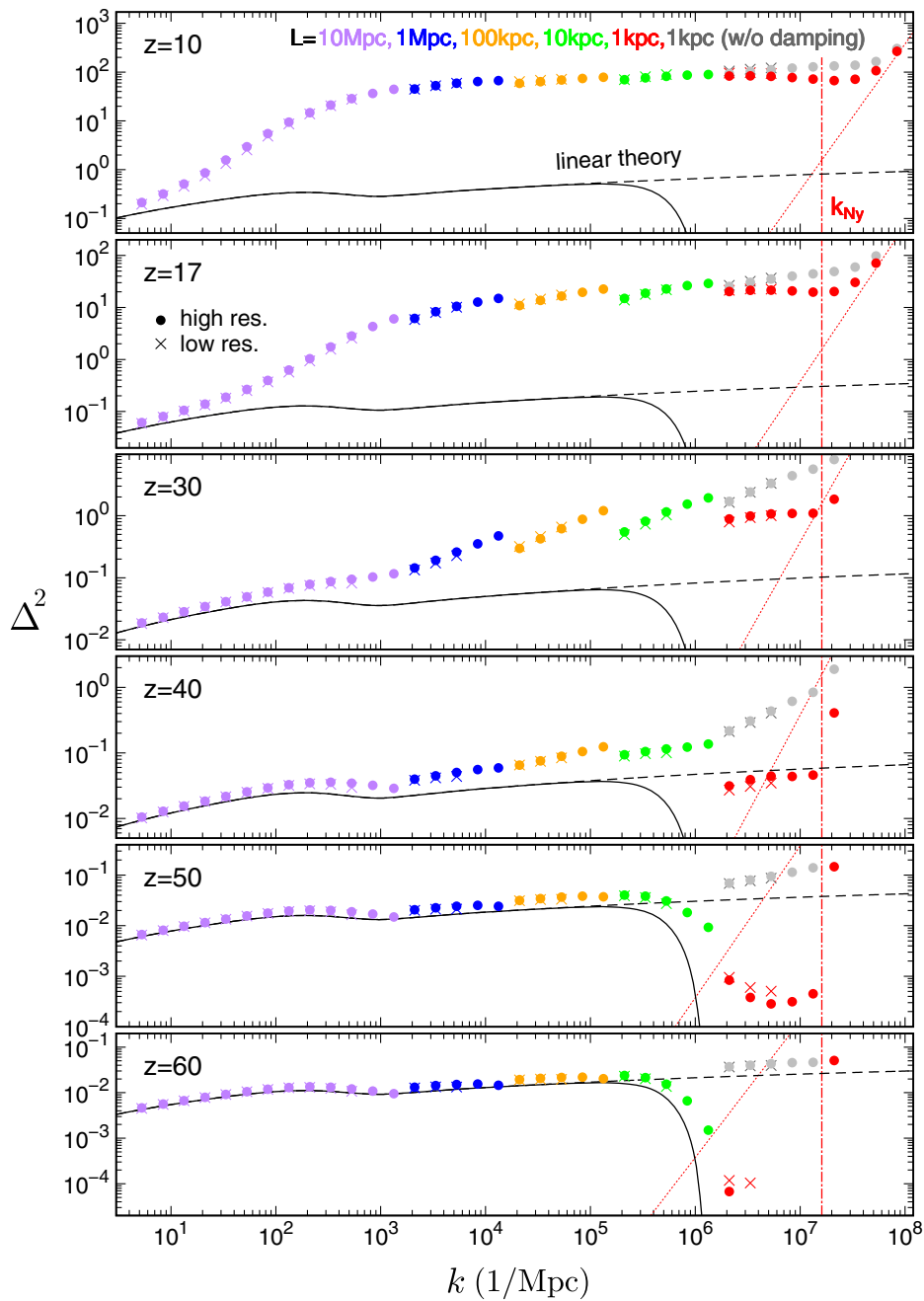
FIG. 2.   Dimensionless matter power spectrum, $\Delta^2(k; z)$, at $z = 10$–60. The symbols denote the simulation results with various box sizes: $L = 10$ Mpc (purple), 1 Mpc (blue), 100 kpc (orange), 10 kpc (green), and 1 kpc (red) from left to right. The gray symbols are the same as the red symbols but do not include the free-streaming damping. The filled circles indicate the HR results with the number of particles $N_p = 5120^3$, whereas the crosses indicate the LR results with $N_p = 2560^3$. Solid curves are the linear theory prediction with the free-streaming damping, and dashed curves are the same without the free-streaming damping. Dotted red lines indicate the shot noise for the red circles. Vertical dot-dashed red lines indicate the Nyquist wave number for the red circles. The discontinuity between the larger and smaller boxes, which is especially prominent at $z = 17$–40, results from the lack of density fluctuations larger than the smaller box size.

means that the simple shot noise term, $\Delta_{\rm sn}$, is not appropriate, which is consistent with the previous remark (e.g., [59]). In fact, the initial condition at $k < k_{\rm Ny}$ does not contain the shot noise.

We comment on the realizable range of k in the simulations. The initial condition includes the linear PS up to $k = k_{\rm Ny}$ but it does not include any power at $k > k_{\rm Ny}$. As time evolves, via the power transfer from large to small

scales, the reliable range extends to higher k ($> k_{\mathrm{Ny}}$), possibly up to the wave number determined by the softening length ϵ ($k_{\mathrm{soft}} = \pi/\epsilon = 20 k_{\mathrm{Ny}}$ in our setting). In the halo model, the maximum reliable k is determined by the smallest halos resolved in the simulation [77]; therefore the mass resolution is also important (a correspondence between the wave number and the halo mass is briefly discussed in Sec. IV. B). The maximum k also depends on the linear spectral index [78]; for a redder spectrum, the reliable k extends further due to the power transfer. In our case of Fig. 2, the red circles approach the shot noise at $k > k_{\mathrm{Ny}}$; therefore the maximum k is primarily determined by the shot noise.

Before concluding this subsection, we would like to comment on the analytical predictions of Δ^2 on the basis of the stable clustering ansatz. Let the linear PS be a single power law, $\Delta_{\mathrm{L}}^2(k; z) \propto P_{\mathrm{L}}(k; z) k^3 \propto k^{n_{\mathrm{L}}+3}$. Then, the corresponding nonlinear PS follows $\Delta^2(k; z) \propto k^{n+3}$ with $n + 3 = 3(n_{\mathrm{L}} + 3)/(n_{\mathrm{L}} + 5)$ [36]. In our case, in Eq. (3), the effective spectral index, $n_{\mathrm{eff}} + 3 \equiv d \ln \Delta_{\mathrm{L}}^2(k)/d \ln k$, ranges from -0.19 to 0.18 at $k = 10^2 - 10^5$ Mpc^{-1}. According to the stable clustering ansatz, the nonlinear spectral index, $n + 3$, ranges from -0.31 to 0.25, which is roughly consistent with the simulation result in the strongly nonlinear regime $\Delta^2 \gtrsim 30$.

B. Cosmological boost factor

The boost factor $B(z)$ can be obtained by integrating the measured $\Delta^2(k; z)$ up to k_{Ny} ($= 1.6 \times 10^7$ Mpc^{-1}) for the HR run. Here, we linearly interpolated the discrete data point of $\Delta^2(k; z)$ in Fig. 2 for the integration in Eq. (2). Figure 3 shows a plot of the resulting $B(z)$. The dashed curve indicates the linear theory prediction obtained analytically from Eqs. (2) and (3): $B_{\mathrm{L}}(z) = 1 + 514(1 + z)^{-2}$. The simulation result agrees with the linear theory at $z \gtrsim 40$ but strongly increases by orders of magnitude at $z \lesssim 40$. The orange curve represents our fit to the simulation result:

$$B_{\mathrm{fit}}(z) = B_{\mathrm{L}}(z) + \frac{4.0 \times 10^4}{(1 + z)^{1.27}} \mathrm{erfc}\left(\frac{1 + z}{18.0}\right). \quad (6)$$

In the high-z limit, Eq. (6) approaches the linear theory prediction, $B_{\mathrm{L}}(z)$. The second term in the equation represents the nonlinear correction (its functional form is the same as the one used in [3], but its fitting parameters are updated). This fitting function agrees with the simulation result within 6.8% at $z = 10$–100. Because the integration in Eq. (2) does not include very small-scale clustering at $k > 1.6 \times 10^7$ Mpc^{-1}, our $B(z)$ represents a lower bound at $z \lesssim 40$. Our result is somewhat smaller than the previous halo-model result for $M_{\mathrm{min}} = 10^{-3} \, M_\odot$ [3]. Note that their result included huge uncertainties as a result of their extrapolation of the halo properties (such as the mass function and density profile) across many orders of magnitude to extremely small scales.
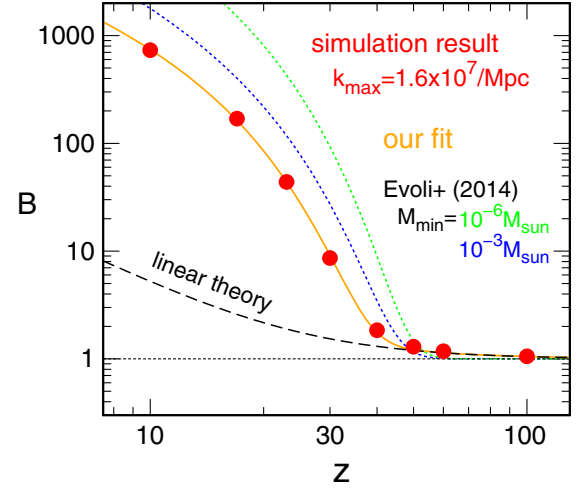

FIG. 3. Boost factor calculated from the simulation results of Δ^2 for the maximum wave number 1.6×10^7 Mpc^{-1} denoted by the red circles. Orange curve represents our fit to the simulation results given in Eq. (6), whereas dashed black curve represents the linear theory prediction. Dotted green and blue curves represent the previous halo-model results [3] for the minimum halo masses $10^{-6} \, M_\odot$ and $10^{-3} \, M_\odot$, respectively.

We include the very small-scale clustering at $k > k_{\mathrm{Ny}}$ in $B(z)$ by extrapolating the measured results of Δ^2. Suppose that $\Delta^2(k; z)$ is a single power law from $k = k_{\mathrm{Ny}}$ to a cutoff wave number k_{cut}, then we have $\Delta^2(k; z) = \Delta^2(k_{\mathrm{Ny}}; z)(k/k_{\mathrm{Ny}})^\gamma$ for $k_{\mathrm{Ny}} \leq k \leq k_{\mathrm{cut}}$ and $\Delta^2(k; z) = 0$ for $k > k_{\mathrm{cut}}$. Figure 2 suggests $\gamma \approx 0$. Then, an additional contribution to $B(z)$, arising from $k > k_{\mathrm{Ny}}$, is written as

$$\Delta B_{\mathrm{fit}}(z) = \Delta^2(k_{\mathrm{Ny}}; z) \ln\left(\frac{k_{\mathrm{cut}}}{k_{\mathrm{Ny}}}\right), \quad \text{for } \gamma = 1$$

$$= \Delta^2(k_{\mathrm{Ny}}; z) \frac{1}{\gamma}\left[\left(\frac{k_{\mathrm{cut}}}{k_{\mathrm{Ny}}}\right)^\gamma - 1\right]. \quad \text{for } \gamma \neq 1 \quad (7)$$

with a fitting function

$$\Delta^2(k_{\mathrm{Ny}}; z) = \frac{4.1 \times 10^2}{(1 + z)^{0.28}} \mathrm{erfc}\left(\frac{1 + z}{16.1}\right). \quad (8)$$

Equation (8) agrees with the simulation results of $\Delta^2(k_{\mathrm{Ny}}; z)$ within 7.2% at $z = 10$–40. By adding ΔB_{fit} to B_{fit} in Eq. (6), one can obtain the boost factor for an arbitrary k_{cut} and γ. For $k_{\mathrm{cut}}/k_{\mathrm{Ny}} = 10$, 100, and 10^3 with $\gamma = 0$, $\Delta B_{\mathrm{fit}}/B_{\mathrm{fit}}$ is less than $0.32, 0.63$, and 0.94, respectively, in the range of $z = 10$–40; therefore, ΔB_{fit} does not exceed B_{fit} even for $k_{\mathrm{cut}} = 10^3 k_{\mathrm{Ny}}$. The cutoff wave number is currently unknown, but it can be estimated from the minimum halo mass in the halo model (see also discussion in Sec. IV. B).

Throughout this paper, the free-streaming scale has been fixed to $k_{\mathrm{fs}} = 10^6$ Mpc^{-1}. Here, we comment on the k_{fs} dependence on the nonlinear $B(z)$. Our simulations cover

wave numbers of up to approximately 10 times larger than k_{fs} even for different k_{fs} values (this is determined by our simulation settings). If the flat spectrum, $\Delta^2(k; z) \approx \text{const.}$, continues at $k > 10k_{fs}$, the resulting $B(z)$ would not converge and would be less sensitive to k_{fs}. Additional simulations are needed to explore the k_{fs} dependence; however, such simulations are beyond the extent of this study and are left as future work.

IV. DISCUSSION

This section discusses the effects of density fluctuations larger than the simulation volume (Sec. IV. A), the cutoff wave number in the halo model (Sec. IV. B), and the baryonic effects on Δ^2 (Sec. IV. C).

A. Density fluctuations larger than the simulation volume

To examine the effects of density fluctuations larger than the box, we computed Δ^2 for various box sizes while retaining the spatial resolution. These additional simulations were run following the same procedure used in Sec. II. C. The result is shown in Fig. 4. The plotting range is from the minimum wave number ($= 2\pi/L$) to the particle Nyquist wave number. Figure 4 indicates that the smaller box simulation underestimates Δ^2 in the nonlinear regime, as expected from the power flow from large to small scales. Here, the missing large-scale power is less important for a bluer spectrum (larger spectral index) and more important for a redder spectrum (smaller spectral index). Because the linear PS in Eq. (3) is red ($n_L + 3 \approx 0$) at $k \gtrsim 10^2 \text{ Mpc}^{-1}$, this effect is prominent. Furthermore, Fig. 4 shows that Δ^2 is steep in the weak nonlinear regime ($1 \lesssim \Delta^2 \lesssim 30$) but becomes shallow in the strong nonlinear regime ($\Delta^2 \gtrsim 30$). This trend is consistent with previous findings (Sec. 5.1 in Ref. [34]).

Next, we calculated the root-mean-square mass fluctuation σ_W within a cubic box in the linear theory. This quantity σ_W needs to be smaller than unity to safely neglect the effect of large-scale fluctuations. The window function for a cubic box of side length L is $W(\mathbf{x}; L) = L^{-3}\Theta(L/2 - |x|) \Theta(L/2 - |y|) \Theta(L/2 - |z|)$, where $\Theta(x)$ is the step function: $\Theta(x) = 1(0)$ for $x \geq 0$ ($x < 0$). Its Fourier transform is $\tilde{W}(\mathbf{k}; L) = \text{sinc}(k_x L/2) \text{sinc}(k_y L/2) \text{sinc}(k_z L/2)$, where $\text{sinc}(x) = \sin x/x$. Accordingly, the linear mass variance can be written as

$$\sigma_W^2(L; z) = \int \frac{d^3\mathbf{k}}{(2\pi)^3} |\tilde{W}(\mathbf{k}; L)|^2 P_L(k; z). \quad (9)$$

This variance is roughly related to Δ_L^2 as $\sigma_W^2(L; z) \approx \Delta_L^2(k = 2\pi/L; z)$. Table II lists the values of σ_W for various L at $z = 10$ [here, $\sigma_W \propto 11/(1+z)$ for an arbitrary z]. Only for $L = 10$ Mpc, the missing large-scale fluctuations are safely negligible; for the other box sizes, they are not. For higher redshifts ($z \geq 17$), because σ_W is smaller, the
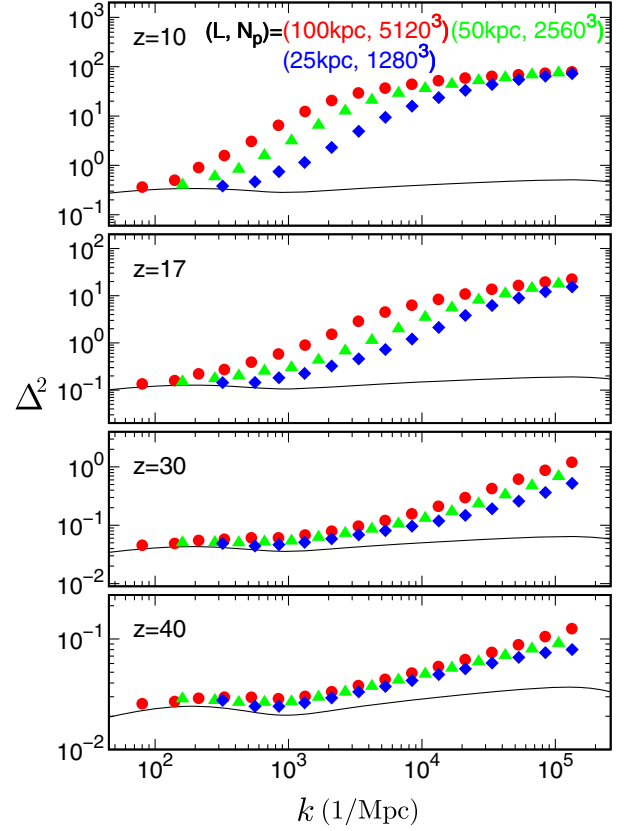

FIG. 4. Dimensionless matter power spectrum $\Delta^2(k; z)$ for various box sizes L with different number of particles N_p but the same spatial resolution: $L = 100$ kpc with $N_p = 5120^3$ (red circles), $L = 50$ kpc with $N_p = 2560^3$ (green triangles), and $L = 25$ kpc with $N_p = 1280^3$ (blue diamonds). Solid curves show the linear theory prediction.

large-scale fluctuations are less important. Note that the linear theory, assumed in Eq. (9), underestimates Δ^2 for $k \gtrsim 10 \text{ Mpc}^{-1}$ at $z = 10$ and, therefore, the obtained σ_W indicates a lower bound.

Density fluctuations larger than the box can be accounted for using the separate universe (SU) technique (e.g., [79–87]). A SU simulation can follow the nonlinear clustering in an over/underdense region of the Universe. In this technique, the mean density of the box, which is usually different from the global mean, is absorbed into the

TABLE II. Root-mean-square mass fluctuation σ_W within a cubic box of side length L, given in Eq. (9), at $z = 10$. Here, linear density fluctuations are assumed.

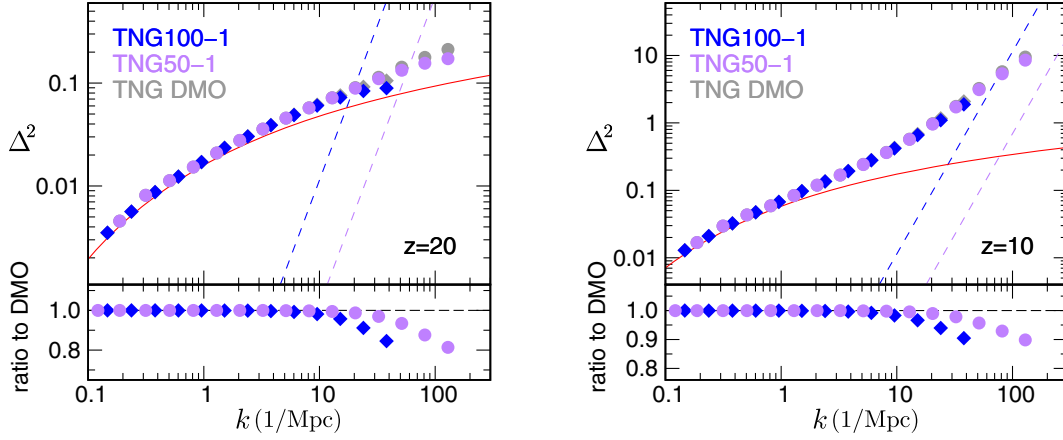| L	σ_W
10 Mpc	0.14
1 Mpc	0.38
100 kpc	0.71
10 kpc	1.09
1 kpc	1.38

FIG. 5.   Nonlinear power spectrum measured from the hydrodynamic simulations including the baryonic processes: TNG100-1 (blue diamonds) and TNG50-1 (purple circles) at $z = 20$ (left) and 10 (right). The gray symbols are the same as the colored ones but are measured from the corresponding DMO runs. Red curve indicates the linear theory, and dashed blue and purple lines indicate the shot noise for TNG100-1 and TNG50-1, respectively. The shot noise is included in the plotted points (i.e., it is not subtracted). The bottom portions of the panels plot the ratio of Δ^2 to the corresponding value for the DMO runs.

change in the cosmological parameters, i.e., the simulation runs under the "local" cosmological parameters. For example, an overdense region corresponds to a spatially closed universe, while an underdense region corresponds to a spatially open universe. The SU simulation can account for the local density contrast, as well as the external tidal field. The SU approach, however, is beyond the scope of this paper and is left as future work.

B. Cutoff wave number in the halo model

This subsection estimates the cutoff wave number $k_{\rm cut}$ of the nonlinear Δ^2 from the typical size of the minimum halo (see, e.g., Sec. 3 of Ref. [19]). The minimum halo mass $M_{h,\rm min}$ is determined by $k_{\rm fs}$ such that $M_{h,\rm min} = (4\pi/3)\bar{\rho}(\pi/k_{\rm fs})^3 \approx 10^{-6}\, M_\odot [k_{\rm fs}/(10^6\,{\rm Mpc}^{-1})]^{-3}$. Because the halo is defined as a spherical region of radius r_v, where the mean density is Δ_v times higher than the background density, we have $M_h = (4\pi r_v^3/3)\bar{\rho}\Delta_v$. Introducing the scale radius of a halo $r_s = r_v/c$, where c is the concentration parameter, we have $k_{\rm cut} = \pi/r_s$. From the above equations, $k_{\rm cut}$ can be written as

$$k_{\rm cut} = c\Delta_v^{1/3}k_{\rm fs},$$
$$= 5.8c\left(\frac{\Delta_v}{200}\right)^{1/3}k_{\rm fs}. \qquad (10)$$

The typical value of c is roughly $c = 1$–2, with a large scatter comparable to its mean, for $M_{h,\rm min}$ [39,40]. Figure 2 suggests that $k_{\rm cut}$ is at least 10 times larger than $k_{\rm fs}$. This means, from Eq. (10), that some halos with $c \gtrsim 2$ and/or substructure in $M_{h,\rm min}$ would contribute to Δ^2 at $k > 10k_{\rm fs}$.

In the halo model, halos with r_s primarily contribute to the nonlinear $\Delta^2(k;z)$ at $k \sim 1/r_s$. In the small-scale limit, but larger than the cutoff scale ($k < k_{\rm cut}$), the spectral index

of Δ^2, $n + 3$, depends on several model ingredients, including the mass function, the concentration parameter, and the linear spectral index $n_{\rm L}$ [e.g., Eq. (4) in Ref. [88]].[3] If $n_{\rm L} + 3 = 0$ and the concentration parameter is independent of the halo mass, then $n + 3 = 0$, which is roughly consistent with our simulation result.

C. Baryonic effects on Δ^2

So far, we have discussed the nonlinear Δ^2 obtained from the dark matter only (DMO) simulations. However, baryonic processes [such as star formation, gas cooling and supernova and active galactic nucleus (AGN) feedback] also affect Δ^2, especially at small scales (e.g., see a recent review by Ref. [89]). This subsection estimates the baryonic effects using public hydrodynamic simulations, IllustrisTNG.[4] The TNG team computed the gravitational evolution, as well as astrophysical processes, using the moving-mesh code AREPO [90]. They ran three sets of simulations in different size cubic boxes, with three mass resolutions for each box size. Here, we used the highest resolution runs in the middle and small box sizes, TNG100-1 [91–95] and TNG50-1 [96,97], respectively. For TNG100-1 and TNG50-1, the box sizes were $L = 75h^{-1}$ and $35h^{-1}$ Mpc, respectively, with the number of particles being $N_p = 1820^3$ and 2160^3, respectively, where N_p was the same for both the baryonic and dark matter particles. The TNG team also performed corresponding DMO runs excluding the baryonic processes, which can be used to observe the impact of baryons on the

---

[3] The spectral index is $n + 3 = [18\beta - \alpha(n_{\rm L} + 3)]/[2(3\beta + 1)]$ where the concentration-mass relation is $c \propto M^{-\beta}$ and the mass function is $dn/dM \propto \nu^\alpha e^{-\nu^2/2}$, with the linear mass variance $\sigma(M) \propto \nu^{-1}$.

[4] https://www.tng-project.org.

small-scale clustering. Their cosmological model parameters were the same as ours. The initial redshift was $z = 127$ for all runs, and the simulation data at $z = 0$–20 were released. Here, we analyze the data at $z = 10$ and 20.

The upper part of the panels in Fig. 5 show plots of Δ^2 calculated from the TNG simulations. The colored symbols are from the simulations with baryons, whereas the gray symbols are from the simulations without baryons. Here, Δ^2 is calculated for the dark matter density (i.e., excluding the baryonic component) even in the baryonic runs because $B(z)$ is determined by the dark matter. The potting range is up to the particle Nyquist wave number. The lower parts of the panels show the ratio of Δ^2 with baryons to Δ^2 without baryons. At larger scales ($k \lesssim 10$ Mpc^{-1}), as expected, the ratio is unity. The baryons slightly suppress Δ^2 by 10%–20% at $k = 10$–200 Mpc^{-1}. The baryonic effects cannot be explored at higher k (> 200 Mpc^{-1}) owing to the finite resolution of the simulations. It is known that at low redshifts ($z \lesssim 3$), baryons suppress the PS at $k = 1$–10 Mpc^{-1} as a result of the AGN feedback but strongly enhance it at $k > 10$ Mpc^{-1} as a result of gas cooling [89]. At high redshift ($z \geq 10$), because the AGN feedback is not effective, the baryon pressure should suppress small-scale clustering at $k > 10$ Mpc^{-1}.

V. CONCLUSIONS

We obtained the cosmological boost factor, $B(z)$, at high redshifts of $z = 10$–100 by integrating the nonlinear PS measured from dedicated high-resolution N-body simulations. To cover a wide range of scales ($k = 1$–10^7 Mpc^{-1}), including the free-streaming scale ($k_{fs} = 10^6$ Mpc^{-1}), we combined five different box-size simulations. Here, our simulations cover wave numbers up to the particle Nyquist frequency of the smallest box, $k_{Ny} = 1.6 \times 10^7$ Mpc^{-1}.

Nonlinear clustering starts at $z \simeq 40$ and enhances the PS by orders of magnitude at $z \lesssim 30$. We found that although free-streaming damping was imposed in the initial PS, this damping feature disappears at late times ($z \lesssim 40$) as a result of the power transfer from large to small scales. Our $B(z)$ result agrees with the linear theory prediction at $z \gtrsim 50$ but is strongly enhanced at $z \lesssim 40$. Our nonlinear $B(z)$ is roughly consistent with, but slightly smaller than, the previous halo-model prediction with $M_{h,\min} = 10^{-3}\ M_{\odot}$ [3]. We provide a simple fitting function for $B(z)$ in Eq. (6). The contribution from the small-scale fluctuations at $k > k_{Ny}$ is also included in our fitting function of $B(z)$, given in Eq. (7), using an extrapolation of the measured results Δ^2 down to the smaller scales; therefore one may obtain $B(z)$ for an arbitrary cutoff wave number. Note that our $B(z)$ result is a lower bound in the nonlinear epoch ($z \lesssim 40$) for the following two reasons: (i) the initial conditions of the simulations do not include density fluctuations smaller than $2\pi/k_{Ny} = 0.39$ pc and (ii) the lack of density fluctuations larger than the simulation volume suppresses nonlinear clustering.

ACKNOWLEDGMENTS

[1] G. Bertone and D. Hooper, Rev. Mod. Phys. **90,** 045002 (2018).

[2] M. Valdés, C. Evoli, A. Mesinger, A. Ferrara, and N. Yoshida, Mon. Not. R. Astron. Soc. **429,** 1705 (2013).

[3] C. Evoli, A. Mesinger, and A. Ferrara, J. Cosmol. Astropart. Phys. 11 (2014) 024.

[4] V. Poulin, P. D. Serpico, and J. Lesgourgues, J. Cosmol. Astropart. Phys. 12 (2015) 041.

[5] H. Liu, T. R. Slatyer, and J. Zavala, Phys. Rev. D **94,** 063507 (2016).

[6] K. Short, J. L. Bernal, A. Raccanelli, L. Verde, and J. Chluba, J. Cosmol. Astropart. Phys. 07 (2020) 020.

[7] J. D. Bowman, A. E. E. Rogers, R. A. Monsalve, T. J. Mozdzen, and N. Mahesh, Nature (London) **555,** 67 (2018).

[8] G. D'Amico, P. Panci, and A. Strumia, Phys. Rev. Lett. **121,** 011103 (2018).

[9] Y. Yang, Phys. Rev. D **98,** 103503 (2018).

[10] K. Cheung, J.-L. Kuo, K.-W. Ng, and Y.-L. S. Tsai, Phys. Lett. B **789,** 137 (2019).

[11] N. Hiroshima, K. Kohri, T. Sekiguchi, and R. Takahashi, arXiv:2103.14810.

[12] P. Ullio, L. Bergström, J. Edsjö, and C. Lacey, Phys. Rev. D **66,** 123502 (2002).

[13] J. E. Taylor and J. Silk, Mon. Not. R. Astron. Soc. **339,** 505 (2003).

[14] S. Ando and E. Komatsu, Phys. Rev. D **73,** 023521 (2006).

[15] M. Cirelli, G. Corcella, A. Hektor, G. Hütsi, M. Kadastik, P. Panci, M. Raidal, F. Sala, and A. Strumia, J. Cosmol. Astropart. Phys. 03 (2011) 051.

[16] M. Shirasaki, S. Horiuchi, and N. Yoshida, Phys. Rev. D **90,** 063502 (2014).

[17] M. Hütten, C. Combet, and D. Maurin, J. Cosmol. Astropart. Phys. 02 (2018) 005.

[18] P. D. Serpico, E. Sefusatti, M. Gustafsson, and G. Zaharijas, Mon. Not. R. Astron. Soc. **421,** L87 (2012).

[19] E. Sefusatti, G. Zaharijas, P. D. Serpico, D. Theurel, and M. Gustafsson, Mon. Not. R. Astron. Soc. **441,** 1861 (2014).

[20] Fermi LAT Collaboration, J. Cosmol. Astropart. Phys. 09 (2015) 008.

[21] A. Cooray and R. Sheth, Phys. Rep. **372,** 1 (2002).

[22] V. Berezinsky, V. Dokuchaev, and Y. Eroshenko, Phys. Rev. D **68,** 103003 (2003).

[23] J. Diemand, M. Kuhlen, and P. Madau, Astrophys. J. **657,** 262 (2007).

[24] V. Springel, S. D. M. White, C. S. Frenk, J. F. Navarro, A. Jenkins, M. Vogelsberger, J. Wang, A. Ludlow, and A. Helmi, Nature (London) **456,** 73 (2008).

[25] J. Zavala and N. Afshordi, Mon. Not. R. Astron. Soc. **457,** 986 (2016).

[26] N. Hiroshima, S. Ando, and T. Ishiyama, Phys. Rev. D **97,** 123002 (2018).

[27] S. Ando, T. Ishiyama, and N. Hiroshima, Galaxies **7,** 68 (2019).

[28] M. Vogelsberger, S. Genel, V. Springel, P. Torrey, D. Sijacki, D. Xu, G. Snyder, D. Nelson, and L. Hernquist, Mon. Not. R. Astron. Soc. **444,** 1518 (2014).

[29] M. Schaller, C. S. Frenk, T. Theuns, F. Calore, G. Bertone, N. Bozorgnia, R. A. Crain, A. Fattahi, J. F. Navarro, T. Sawala, and J. Schaye, Mon. Not. R. Astron. Soc. **455,** 4442 (2016).

[30] K. T. E. Chua, A. Pillepich, M. Vogelsberger, and L. Hernquist, Mon. Not. R. Astron. Soc. **484,** 476 (2019).

[31] K. J. Mack, Mon. Not. R. Astron. Soc. **439,** 2728 (2014).

[32] M. A. Sánchez-Conde and F. Prada, Mon. Not. R. Astron. Soc. **442,** 2271 (2014).

[33] Á. Moliné, M. A. Sánchez-Conde, S. Palomares-Ruiz, and F. Prada, Mon. Not. R. Astron. Soc. **466,** 4974 (2017).

[34] R. E. Smith, J. A. Peacock, A. Jenkins, S. D. M. White, C. S. Frenk, F. R. Pearce, P. A. Thomas, G. Efstathiou, and H. M. P. Couchman, Mon. Not. R. Astron. Soc. **341,** 1311 (2003).

[35] R. Takahashi, M. Sato, T. Nishimichi, A. Taruya, and M. Oguri, Astrophys. J. **761,** 152 (2012).

[36] P. J. E. Peebles, *The large-scale structure of the universe* (Princeton University Press, 1980).

[37] V. Springel, S. D. M. White, A. Jenkins, C. S. Frenk, N. Yoshida, L. Gao, J. Navarro, R. Thacker, D. Croton, J. Helly, J. A. Peacock, S. Cole, P. Thomas, H. Couchman, A. Evrard, J. Colberg, and F. Pearce, Nature (London) **435,** 629 (2005).

[38] M. Boylan-Kolchin, V. Springel, S. D. M. White, A. Jenkins, and G. Lemson, Mon. Not. R. Astron. Soc. **398,** 1150 (2009).

[39] J. Diemand, B. Moore, and J. Stadel, Nature (London) **433,** 389 (2005).

[40] T. Ishiyama, Astrophys. J. **788,** 27 (2014).

[41] A. Schneider, Mon. Not. R. Astron. Soc. **451,** 3117 (2015).

[42] J. Wang, S. Bose, C. S. Frenk, L. Gao, A. Jenkins, V. Springel, and S. D. M. White, Nature (London) **585,** 39 (2020).

[43] Planck Collaboration, Astron. Astrophys. **594,** A13 (2016).

[44] K. Yamamoto, N. Sugiyama, and H. Sato, Astrophys. J. **501,** 442 (1998).

[45] K. Yamamoto (private communication).

[46] A. Lewis, A. Challinor, and A. Lasenby, Astrophys. J. **538,** 473 (2000).

[47] J. M. Bardeen, J. R. Bond, N. Kaiser, and A. S. Szalay, Astrophys. J. **304,** 15 (1986).

[48] W. Hu and N. Sugiyama, Astrophys. J. **471,** 542 (1996).

[49] A. M. Green, S. Hofmann, and D. J. Schwarz, Mon. Not. R. Astron. Soc. **353,** L23 (2004).

[50] A. Loeb and M. Zaldarriaga, Phys. Rev. D **71,** 103520 (2005).

[51] Planck Collaboration, Astron. Astrophys. **641,** A10 (2020).

[52] M. Crocce, S. Pueblas, and R. Scoccimarro, Mon. Not. R. Astron. Soc. **373,** 369 (2006).

[53] T. Nishimichi, A. Shirata, A. Taruya, K. Yahata, S. Saito, Y. Suto, R. Takahashi, N. Yoshida, T. Matsubara, N. Sugiyama, I. Kayo, Y. Jing, and K. Yoshikawa, Publ. Astron. Soc. Jpn. **61,** 321 (2009).

[54] P. Valageas and T. Nishimichi, Astron. Astrophys. **527,** A87 (2011).

[55] T. Ishiyama, T. Fukushige, and J. Makino, Publ. Astron. Soc. Jpn. **61,** 1319 (2009).

[56] Y. P. Jing, Astrophys. J. **620,** 559 (2005).

[57] E. Sefusatti, M. Crocce, R. Scoccimarro, and H. M. P. Couchman, Mon. Not. R. Astron. Soc. **460,** 3624 (2016).

[58] A. Jenkins, C. S. Frenk, F. R. Pearce, P. A. Thomas, J. M. Colberg, S. D. M. White, H. M. P. Couchman, J. A. Peacock, G. Efstathiou, and A. H. Nelson, Astrophys. J. **499,** 20 (1998).

[59] K. Heitmann, M. White, C. Wagner, S. Habib, and D. Higdon, Astrophys. J. **715,** 104 (2010).

[60] A. Pontzen, A. Slosar, N. Roth, and H. V. Peiris, Phys. Rev. D **93,** 103519 (2016).

[61] R. E. Angulo and A. Pontzen, Mon. Not. R. Astron. Soc. **462,** L1 (2016).

[62] J. Wang and S. D. M. White, Mon. Not. R. Astron. Soc. **380,** 93 (2007).

[63] R. E. Angulo, O. Hahn, and T. Abel, Mon. Not. R. Astron. Soc. **434,** 3337 (2013).

[64] A. Schneider, R. E. Smith, and D. Reed, Mon. Not. R. Astron. Soc. **433,** 1573 (2013).

[65] T. Ishiyama and S. Ando, Mon. Not. R. Astron. Soc. **492,** 3662 (2020).

[66] J. S. Bagla and T. Padmanabhan, Mon. Not. R. Astron. Soc. **286,** 1023 (1997).

[67] T. Padmanabhan and S. Ray, Mon. Not. R. Astron. Soc. **372,** L53 (2006).

[68] J. S. Bagla and J. Prasad, Mon. Not. R. Astron. Soc. **393,** 607 (2009).

[69] M. C. Neyrinck and L. F. Yang, Mon. Not. R. Astron. Soc. **433,** 1628 (2013).

[70] T. Nishimichi, F. Bernardeau, and A. Taruya, Phys. Lett. B **762,** 247 (2016).

[71] B. Little, D. H. Weinberg, and C. Park, Mon. Not. R. Astron. Soc. **253,** 295 (1991).

[72] M. White and R. A. C. Croft, Astrophys. J. **539,** 497 (2000).

[73] R. E. Smith and K. Markovic, Phys. Rev. D **84**, 063507 (2011).
[74] M. Viel, K. Marković, M. Baldi, and J. Weller, Mon. Not. R. Astron. Soc. **421**, 50 (2012).
[75] K. T. Inoue, R. Takahashi, T. Takahashi, and T. Ishiyama, Mon. Not. R. Astron. Soc. **448**, 2704 (2015).
[76] M. Leo, C. M. Baugh, B. Li, and S. Pascoli, J. Cosmol. Astropart. Phys. 08 (2018) 001.
[77] T. Hamana, N. Yoshida, and Y. Suto, Astrophys. J. **568**, 455 (2002).
[78] S. Maleubre, D. Eisenstein, L. H. Garrison, and M. Joyce, arXiv:2109.04397.
[79] E. Sirko, Astrophys. J. **634**, 728 (2005).
[80] M. Takada and W. Hu, Phys. Rev. D **87**, 123504 (2013).
[81] Y. Li, W. Hu, and M. Takada, Phys. Rev. D **89**, 083519 (2014).
[82] C. Wagner, F. Schmidt, C. T. Chiang, and E. Komatsu, Mon. Not. R. Astron. Soc. **448**, L11 (2015).
[83] T. Baldauf, U. Seljak, L. Senatore, and M. Zaldarriaga, J. Cosmol. Astropart. Phys. 09 (2016) 007.
[84] R. Takahashi, T. Nishimichi, M. Takada, M. Shirasaki, and K. Shiroyama, Mon. Not. R. Astron. Soc. **482**, 4253 (2019).
[85] A. Barreira, D. Nelson, A. Pillepich, V. Springel, F. Schmidt, R. Pakmor, L. Hernquist, and M. Vogelsberger, Mon. Not. R. Astron. Soc. **488**, 2079 (2019).
[86] S. Masaki, T. Nishimichi, and M. Takada, Mon. Not. R. Astron. Soc. **496**, 483 (2020).
[87] K. Akitsu, Y. Li, and T. Okumura, J. Cosmol. Astropart. Phys. 04 (2021) 041.
[88] C.-P. Ma and J. N. Fry, Astrophys. J. **538**, L107 (2000).
[89] N. E. Chisari, A. J. Mead, S. Joudaki, P. G. Ferreira, A. Schneider, J. Mohr, T. Tröster, D. Alonso, I. G. McCarthy, S. Martin-Alvarez, J. Devriendt, A. Slyz, and M. P. van Daalen, Open J. Astrophys. **2**, 4 (2019).
[90] V. Springel, Mon. Not. R. Astron. Soc. **401**, 791 (2010).
[91] F. Marinacci, M. Vogelsberger, R. Pakmor, P. Torrey, V. Springel, L. Hernquist, D. Nelson, R. Weinberger, A. Pillepich, J. Naiman, and S. Genel, Mon. Not. R. Astron. Soc. **480**, 5113 (2018).
[92] V. Springel, R. Pakmor, A. Pillepich, R. Weinberger, D. Nelson, L. Hernquist, M. Vogelsberger, S. Genel, P. Torrey, F. Marinacci, and J. Naiman, Mon. Not. R. Astron. Soc. **475**, 676 (2018).
[93] A. Pillepich, D. Nelson, L. Hernquist, V. Springel, R. Pakmor, P. Torrey, R. Weinberger, S. Genel, J. Naiman, F. Marinacci, and M. Vogelsberger, Mon. Not. R. Astron. Soc. **475**, 648 (2018).
[94] D. Nelson, A. Pillepich, V. Springel, R. Weinberger, L. Hernquist, R. Pakmor, S. Genel, P. Torrey, M. Vogelsberger, G. Kauffmann, F. Marinacci, and J. Naiman, Mon. Not. R. Astron. Soc. **475**, 624 (2018).
[95] J. P. Naiman, A. Pillepich, V. Springel, E. Ramirez-Ruiz, P. Torrey, M. Vogelsberger, R. Pakmor, D. Nelson, F. Marinacci, L. Hernquist, R. Weinberger, and S. Genel, Mon. Not. R. Astron. Soc. **477**, 1206 (2018).
[96] D. Nelson, A. Pillepich, V. Springel, R. Pakmor, R. Weinberger, S. Genel, P. Torrey, M. Vogelsberger, F. Marinacci, and L. Hernquist, Mon. Not. R. Astron. Soc. **490**, 3234 (2019).
[97] A. Pillepich, D. Nelson, V. Springel, R. Pakmor, P. Torrey, R. Weinberger, M. Vogelsberger, F. Marinacci, S. Genel, A. van der Wel, and L. Hernquist, Mon. Not. R. Astron. Soc. **490**, 3196 (2019).